

On-off and proportional–integral controller for a morphing wing. Part 2: Control validation – numerical simulations and experimental tests

T L Grigorie¹, A V Popov¹, R M Botez^{1*}, M Mamou², and Y Mébarki²

¹École de Technologie Supérieure, Montréal, Québec H3C 1K3, Canada

²National Research Council, Ottawa, Ontario, Canada

The manuscript was received on 27 August 2010 and was accepted after revision for publication on 4 April 2011.

DOI: 10.1177/0954410011408271

Abstract: The second part of this article describes the numerical simulation and experimental validations of actuators control system for a morphing wing application, which was developed and designed in the first part of this article. After the description of the finally adopted control architecture, the validation for the non-linear system model is presented. First, the integrated controller is validated numerically with MATLAB/Simulink software, followed by a physical implementation of the control and experimental validation in the wind tunnel. To implement the controller on the physical model, two programmable switching power supplies, AMREL SPS100-33, and Quanser Q8 data acquisition card were used. The inputs of the data acquisition card were the two signals issued by the linear variable differential transformer potentiometers, indicating the positions of the actuators, and the six signals recorded by thermocouples installed on the SMA wires. The acquisition board output channels were used to control the required power supply to obtain the desired skin deflections. The control experimental validation was performed first on a bench test and then in the wind tunnel test. A number of optimized airfoil shapes, used in the design phase, were translated into actuators vertical displacements which were used as input signals for the controller. In the wind tunnel tests, a comparative study was realized around the transition point position for the reference airfoil and for each optimized airfoil.

Keywords: morphing wing, actuators control system, numerical simulation, bench testing, wind tunnel validation test

1 INTRODUCTION

The spectacular and continuous evolution of the aerospace engineering domain was specially highlighted in the past years through the onboard avionics equipments and systems technology development. However, at the same time, the two related sub-domains, propulsion systems, and aircraft structures, in parallel, registered very important discoveries,

usually not well appreciated by general public. Thus, to become more visible, the concept of green aircraft was launched in the aerospace industries to reorient research towards noise, fuel emission, and fuel consumption reduction. This concept is a consequence of the future predictions on more air traffic for the next 20 years. Therefore, both environmental and economic pressures will affect aerospace industries to focus on increasing aircraft performances and reduce emissions. In order to meet those challenges, aircrafts with new concepts will be designed and new technologies will be developed and investigated. This will be followed by a thorough validation and

*Corresponding author: École de Technologie Supérieure, Montréal, Québec H3C 1K3, Canada.
email: ruxandra.botez@etsmtl.ca

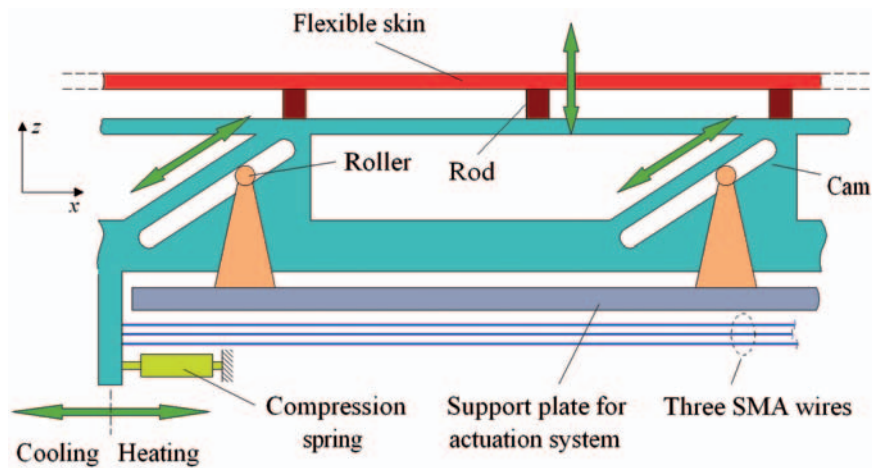


Fig. 1 The actuation mechanism concept

integration of various new technologies and solutions to the most critical aircraft components such as the cabin, wing, power plant system, and fuselage; multi-disciplinary investigations already explore the different associated aspects of aerodynamics, acoustics, materials, structure, engines, and systems. The objectives of these investigations are to ensure an improved product quality and affordability, while meeting the tightening environmental constraints (fuel emission and noise), with a vision of global efficiency of the air transport system.

Within this context, aiming the reduction of fuel emission, this research study is focused on the development of a new morphing wing concept to optimally adapt the aircraft under various flow conditions to ensure a low viscous drag force [1–7]. The main objective of this study is to develop an actuation control concept for a new morphing mechanism using smart materials, like shape memory alloy (SMA), as actuators. The main role of the actuators is to modify the upper surface of the wing made of a flexible material such that the laminar-to-turbulent flow transition point moves close to the wing trailing edge, thus causing less viscous drag. This concept is developed to operate under various flow conditions by changing the wing shape.

The chosen model is a rectangular plan wing based on the airfoil section WTEA-TE1. The wing has a chord c of 0.5 m and a span of 0.9 m. The wing model was equipped with a flexible skin made of composite materials (layers of carbon and Kevlar fibres in a resin matrix) subject to two actuation lines. For skin deformation, each actuation line uses SMAs wires as actuators.

In the first part of this article, a control for the actuation lines of the morphing wing system was designed

to handle 35 optimized airfoils for 35 different flow conditions, using five Mach numbers (from 0.2 to 0.3 with an increment of 0.025) and seven angles of attack (from -1° to 2° with an increment of -0.5°) combinations.

The actuation mechanism consists of two actuation lines having three SMA actuator wires (1.8 m in length each), and a cam having two degrees-of-transition motions; it moves horizontally and vertically relative to the structure (on the x -axis, as shown in Fig. 1).

The cam causes the vertical movement of a rod resulting from the sliding of the rollers along the cam slots. A force recall is executed by a gas spring. The horizontal displacement of each actuator is converted into a vertical displacement at a rate 3:1, which causes the horizontal stroke of x mm to be converted into a vertical stroke $z = x/3$, resulting in a cam factor of $c_f = 1/3$. Therefore, for approximately 8 mm maximum vertical displacement, obtained from the optimized airfoils, a 24 mm maximum horizontal displacement should be achieved by the actuation lines.

The designed controller controls the SMA actuators in terms of supplying electrical current to cancel the deviation between the required values for vertical displacements (corresponding to the optimized airfoils) and the real measured values, obtained from two position transducers (Fig. 2).

The final chosen configuration of the integrated controller (discussed in the first part of this article) was a combination of a bipositional controller (particularly an on-off one) and a proportional-integral (PI) controller, due to the two heating and cooling phases of the SMA wires interconnection. The resulted controller is designed to behave like a switch between

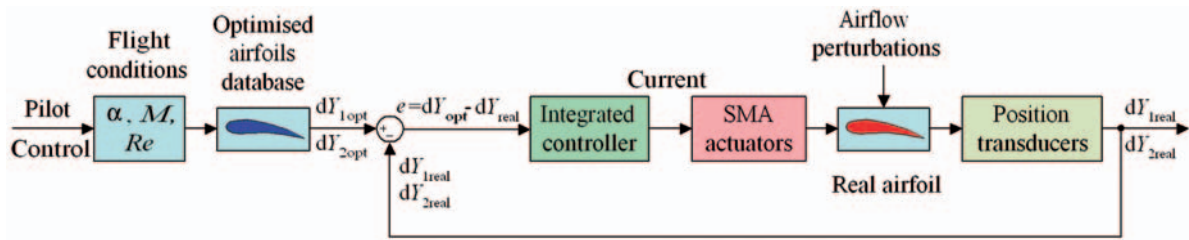


Fig. 2 Operating schema of the SMA actuators control

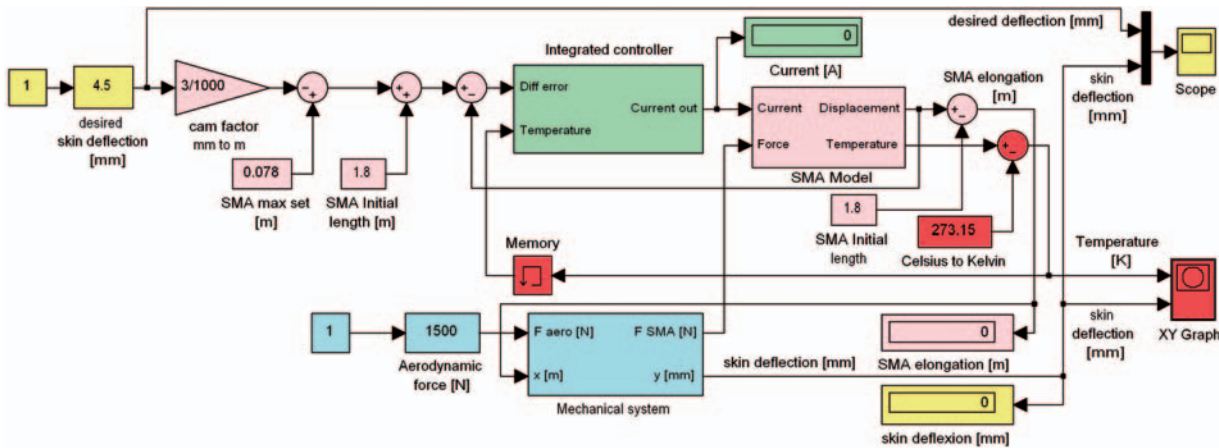


Fig. 3 The simulation model for the controlled SMA actuator with the non-linear model

cooling and heating phases, situations where the output current is 0 A or it is controlled by a law of PI type as follows

$$i(t) = \begin{cases} 0, & \text{if } e \leq 0, \\ 1792.8 \cdot e(t) + 787 \cdot \int e(t) \cdot dt, & \text{if } e > 0. \end{cases} \quad (1)$$

where e is the operating error (Fig. 2).

This article is organized as follows. Section 2 presents the MATLAB/Simulink implementation of the morphing model and the control validation through numerical simulations. Section 3 describes about the fully physical open-loop morphing wing and interprets the validation results obtained in a bench test. Results obtained in a wind tunnel validation test are presented in section 4 to demonstrate the complete operation of the developed integrated controller. Finally, in section 5, conclusions are drawn from the numerical simulation and experimental validation tests shown.

2 CONTROL VALIDATION FOR THE GENERAL MODEL OF THE SYSTEM (THE NON-LINEAR ONE) USING NUMERICAL SIMULATION

Introducing the controller in a general block scheme, with the non-linear SMA model, the Simulink model

illustrated in Fig. 3 was obtained for the skin control of the SMA actuators (Fig. 2). The input variable of the scheme is the desired skin deflection and the output the real skin deflection. Information about the supplying current, the force loading the SMA actuators, which is a function of temperature and elongation, can be extracted from the scheme.

As displayed in Fig. 4, the ‘Integrated controller’ block contains the implementation of the law described by equation (1) and the preliminary observations related to the SMA actuators’ physical limitations in terms of temperature and supplying currents. The block has as an input as the control error (the difference between the desired and the obtained displacements) and the SMA wire temperatures. The output is the controlled electrical current applied on the SMA actuators. There are two switches in the scheme; the first one chooses one of the two options in the control law (1) and the second one switches the electrical current value to 0 A when the SMA temperature value is over the imposed limit. In addition, a current saturation block is used to prevent the current increase over the physical limit supported by the actuation SMA wires.

Loading the simulated model with different values for aerodynamic force F_{aero} (1000, 1500, and 1800 N), the actuators characteristics exemplified in Figs 5 to 7

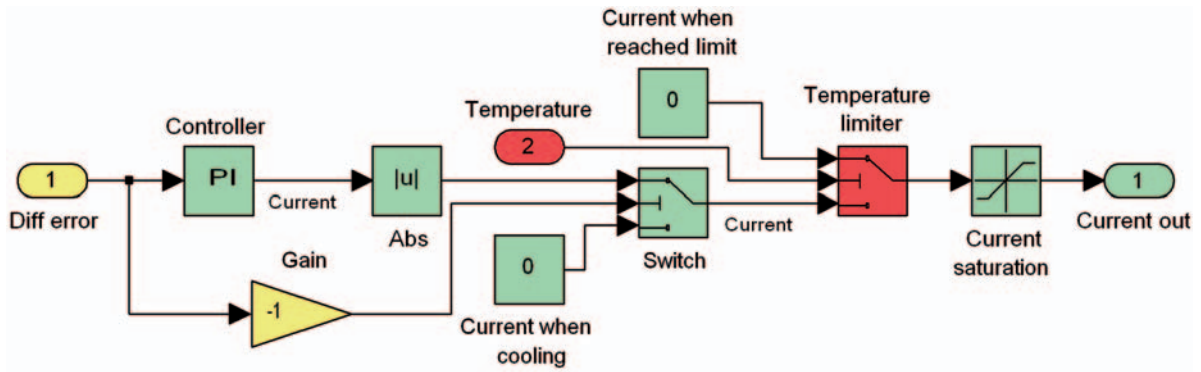


Fig. 4 'Integrated controller' block in Simulink

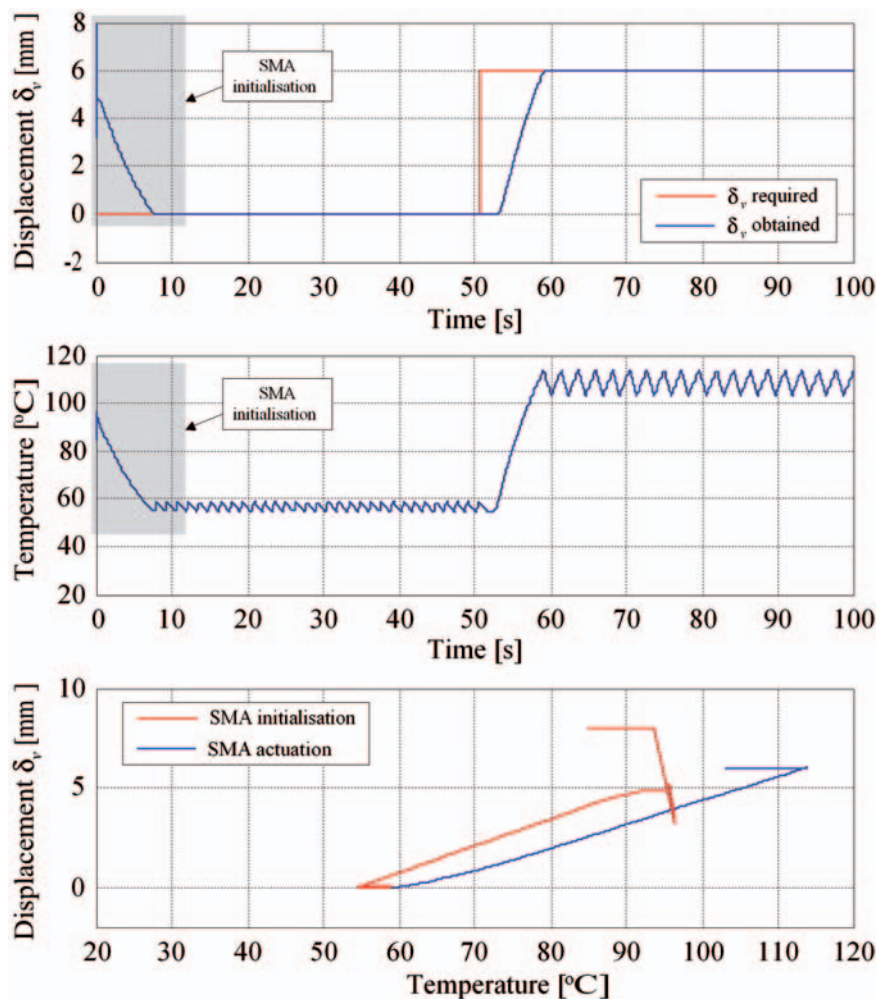


Fig. 5 System response for a step input when $F_{aero} = 1000$ N

are obtained for a 6 mm step desired skin deflection (δ_v). First of all, from these figures, it can be observed that the controller works well; the transition to the desired steady state is significantly improved through the integration of the two options of the control law in equation (1). The oscillation amplitudes were

reduced and the observed oscillations in the SMA temperatures around the steady state were only those due to the thermal inertia of the smart material. The transition time from 0 mm to the steady state values decreased from 20–25 s to approximately 5 s. Another observation can be made relative to the

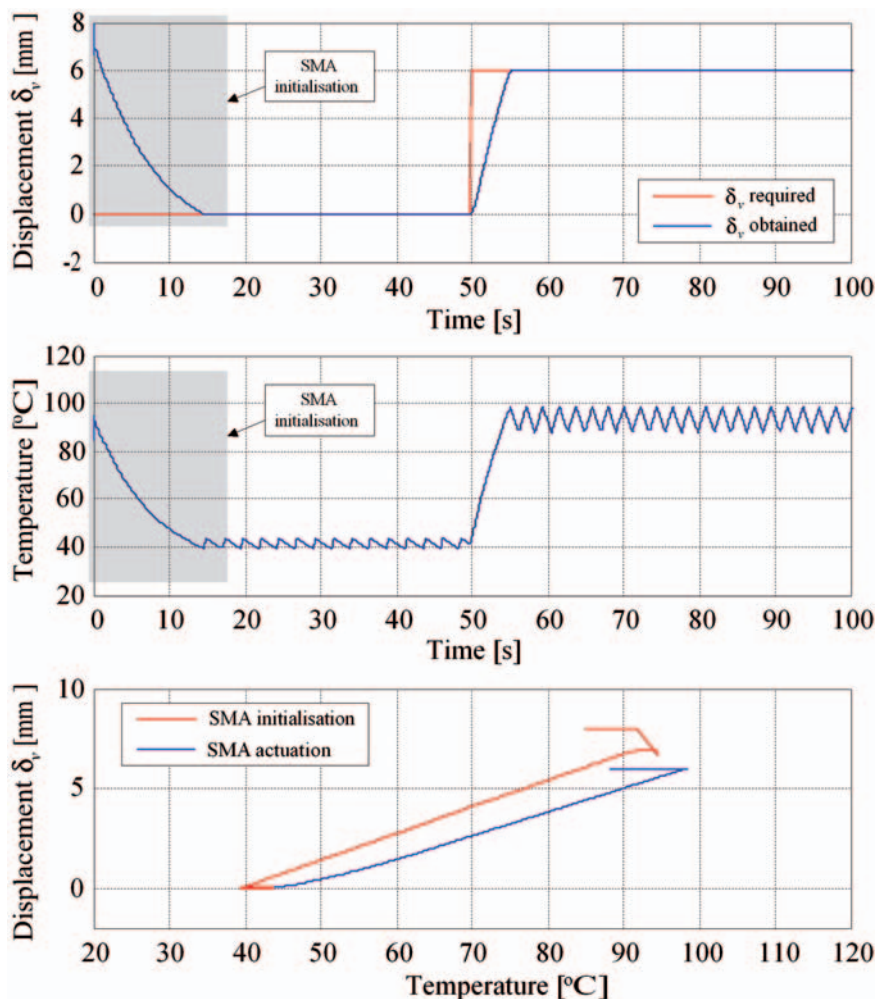


Fig. 6 System response for a step input when $F_{\text{aero}} = 1500$ N

values of the aerodynamic force F_{aero} , which is the determination of the load force of the SMA (F_{SMA}). As already noted, the pretension force of the gas spring was chosen to be 1500 N. In accordance with equation (2), the aerodynamic force value is reflected with a 1:3 ratio in the F_{SMA} calculus. For a F_{aero} value under 1400 N, the F_{SMA} value in the steady state of the initialization phase is larger than 1050 N and the deformation starts with a time delay of approximately 3 s when $F_{\text{aero}} = 1000$ N (Fig. 5). This delay disappeared when the F_{SMA} value, in the steady state of the initialization phase, is less than 1050 N (Figs 6 and 7, where $F_{\text{aero}} = 1500$ and 1800 N, respectively). Another positive effect related to the increase in F_{aero} is the lowering of the work temperatures for the SMA actuators (over 110°C for $F_{\text{aero}} = 1000$ N and under 90°C for $F_{\text{aero}} = 1800$ N). The advantage of lowering the temperature is twofold: (1) a lower temperature allows an actuator to cool more quickly and (2) the interaction between the actuators and the other parts of the physical model will be within nominal limits.

From another standpoint of view, the F_{aero} increase produces an increase in the initialization phase (from 8 s when $F_{\text{aero}} = 1000$ N to 27 s when $F_{\text{aero}} = 1800$ N). In the simulations, it was observed that a high F_{aero} value produces a low load force F_{SMA} and, at this point, the actuators do not function properly. Therefore, by estimating the aerodynamic forces for all 35 studied flight conditions and 35 optimized airfoils, a compromise must be made to balance the aerodynamic forces with the preloaded forces of the gas spring. In general, the preloaded forces on the gas springs in the two actuation lines must be valid for all the studied cases.

Applying to the input of the controlled actuator a successive steps signal, the characteristics shown in Figs 8 and 9 were obtained. Two cases of aerodynamic forces load were considered; $F_{\text{aero}} = 1500$ N (Fig. 8) and $F_{\text{aero}} = 1800$ N (Fig. 9). The numerical simulations confirm again that the obtained integrated controller works well, and the variant of the on-off controller combined with a well-tuned PI controller give very

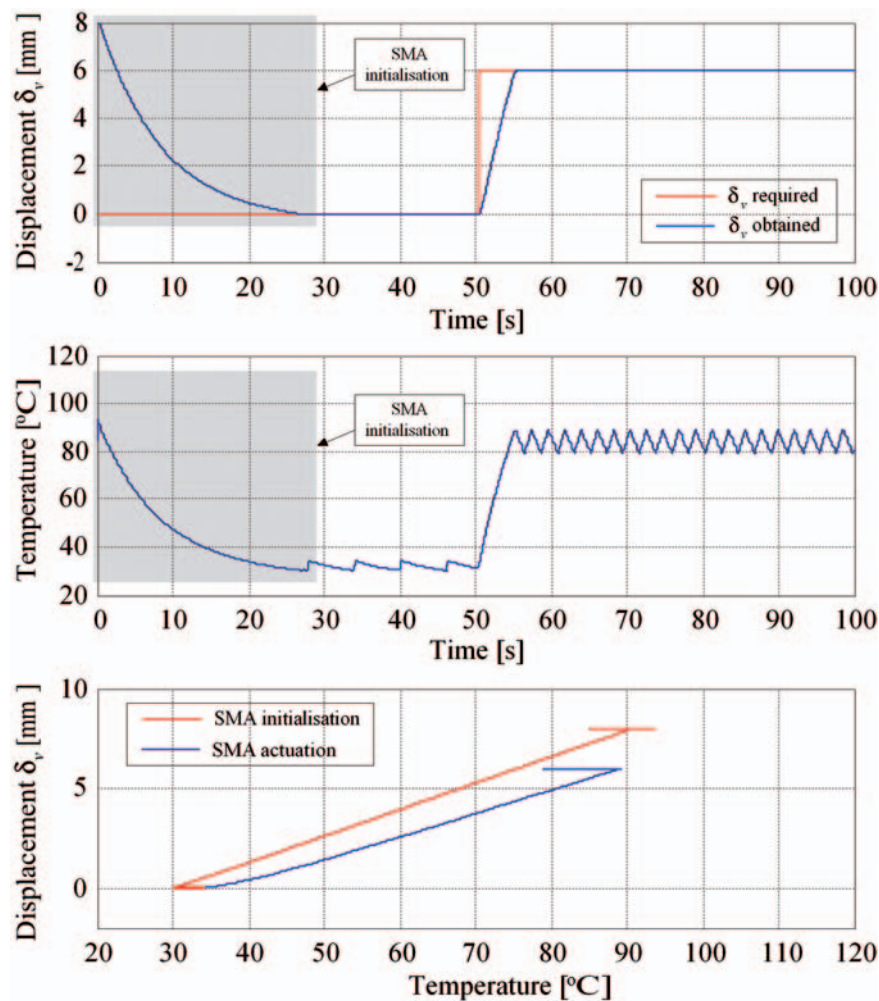


Fig. 7 System response for a step input when $F_{\text{aero}} = 1800 \text{ N}$

good results in both phases (heating and cooling) of the SMA actuators. A few seconds of lateness of the cooling phase *vis-à-vis* of the heating phase is observed. Also, it can be noticed that the amplitude of the temperature oscillations is getting higher with the actuation temperature increase and it depends on the SMA load force. For $F_{\text{aero}} = 1500 \text{ N}$, the F_{SMA} varies between 1 and 1.33 kN, and for $F_{\text{aero}} = 1800 \text{ N}$ between 0.9 and 1.23 kN. Correlating the conclusions from Figs 5 to 9, relying on the load force results, it seems that the actuators work well when they are heavily loaded ($F_{\text{pretension}}$ higher so F_{SMA} higher) below the non-deformable load limit.

3 PHYSICAL MORPHING WING MODEL IMPLEMENTATION AND ACTUATORS' INTEGRATED CONTROLLER BENCH TESTING

Based on the theoretical and numerical simulation results, two Programmable Switching Power

Supplies AMREL SPS100-33, controlled by MATLAB/Simulink through a Quanser Q8 data acquisition card, were used in the set displayed in Fig. 10 to implement the controller model [8–10]. The power supplies have RS-232 and GPIB IEEE-488 as standard features and technical characteristics that include: Power 3.3 kW, Voltage (dc) 0–100 V, Current (dc) 0–33 A. The Q8 data acquisition card has eight single-ended analogue inputs with 14-bit resolution. All eight channels can be sampled simultaneously at 100 kHz, with an A/D conversion times of 2.4 μs /channel. Simultaneous sampling and sampling frequencies of up to 350 kHz for two channels can be performed. Also, the Q8 card is equipped with eight analogue outputs, software programmable voltage ranges and simultaneous update capability with an 8 μs settling time over the full scale (20 V). The morphing wing system in the bench test runs is shown in Fig. 11.

The acquisition board was connected to a PC and programmed via MATLAB/Simulink R2006b and

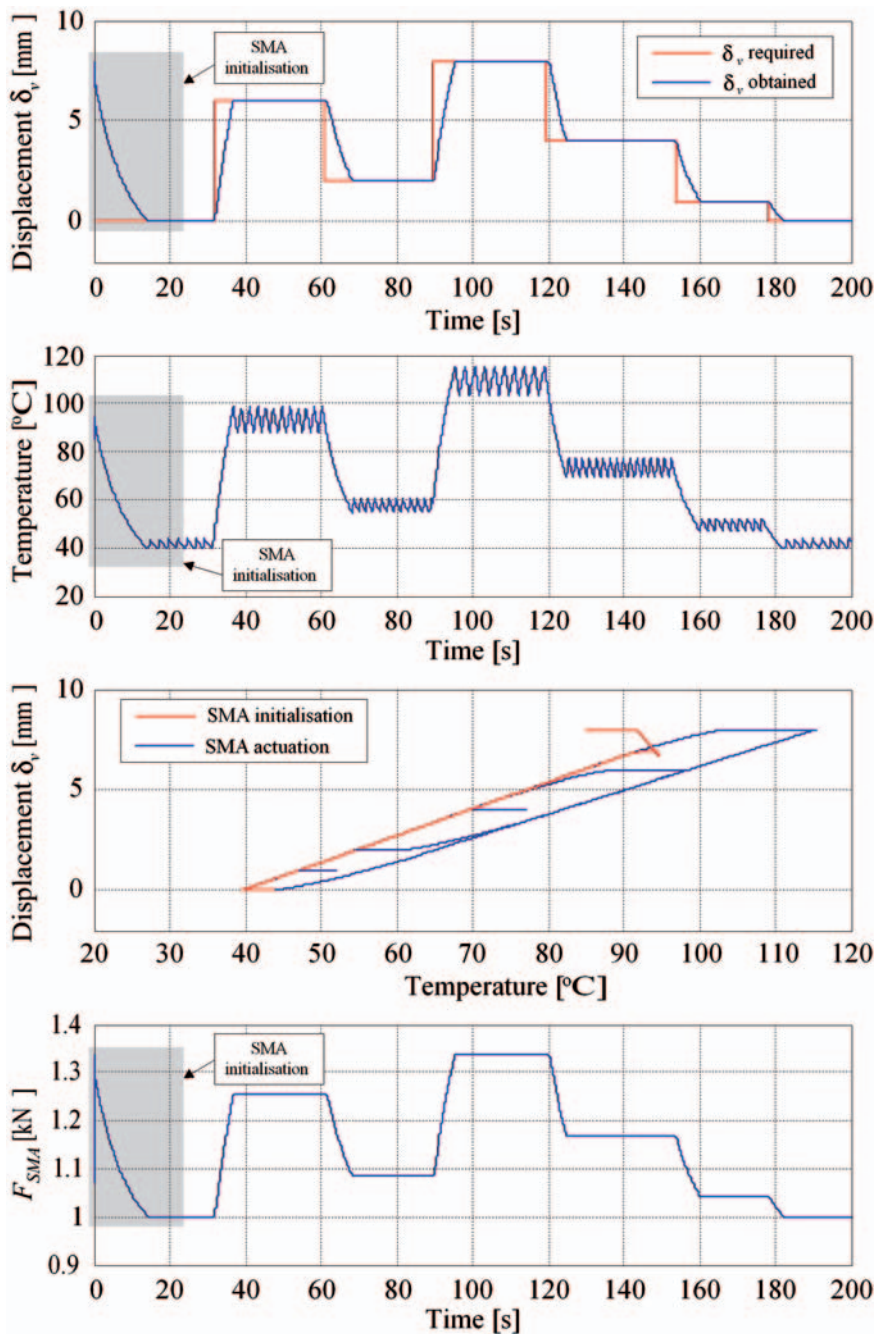


Fig. 8 Response for a successive step input, $F_{aero} = 1500$ N

WinCon 5.2 (Fig. 12). The input were two signals from the linear variable differential transducer (LVDT) potentiometers, which indicate the positions of the SMA actuators, and six signals from thermocouples installed on each of the SMA wire components. The acquisition sampling time was set to 10 μ s. The output channels of the acquisition board were used to control each power supply through analogue/external control by means of a DB-15 I/O connector. As seen from Fig. 13, modelling the

‘SMA1’ block in Fig. 12, the current supplied to the actuator was limited at 10 A maximum, and the control signal was set to be 0–0.6061 V (maximum voltage for the power supply is 2 V for a 33 A current supply). The gas springs that maintain the SMA wires in tension have a preloaded value of 225 lbs (1000 N), since aerodynamic loads are absent in the bench test.

The operation principle of the physically implemented controller is relatively simple. The initial

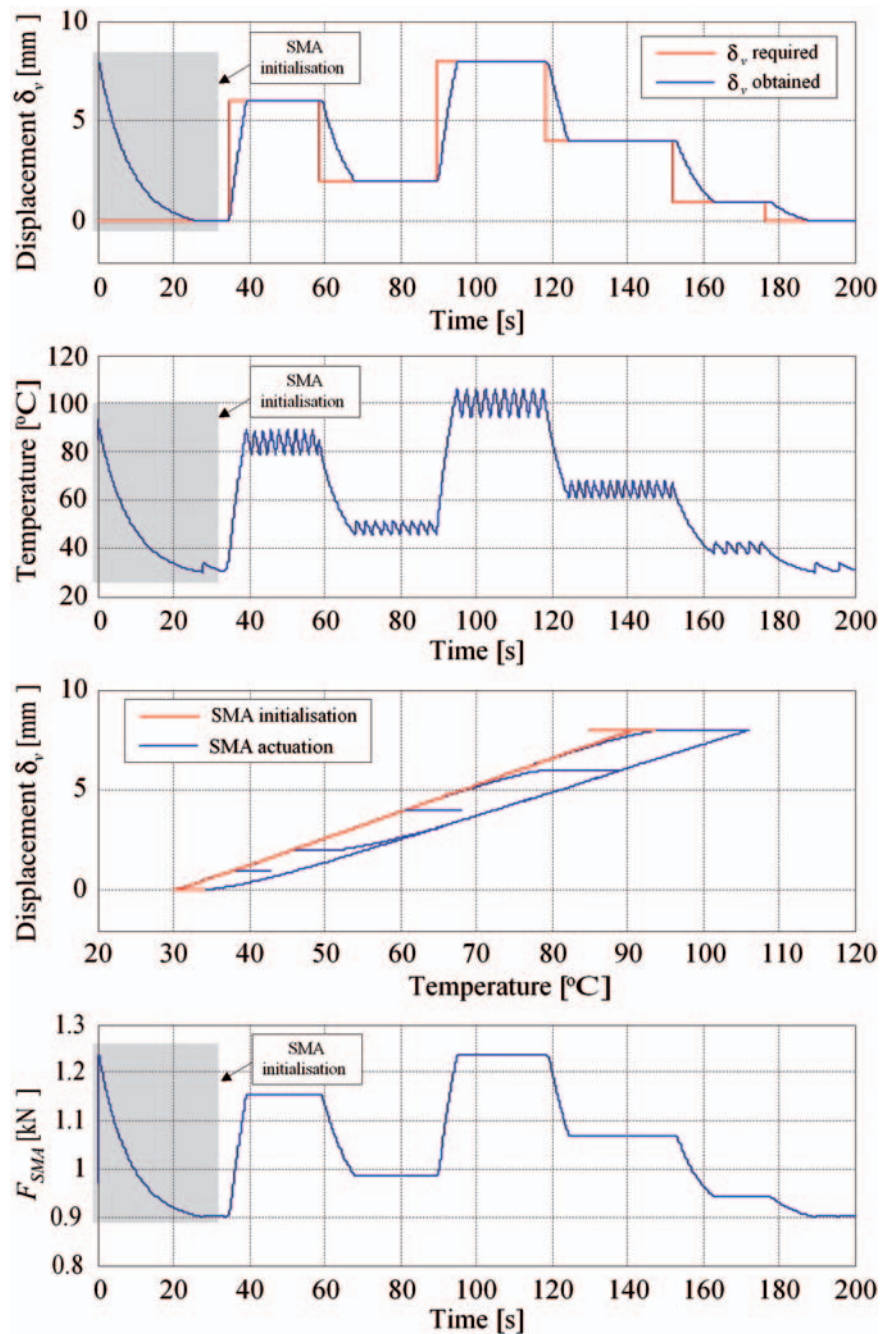


Fig. 9 Response for a successive step input, $F_{\text{aero}} = 1800 \text{ N}$

input, which is the optimized airfoil for any flow condition, is chosen manually by the operator from the computer database through a user interface. Then, the displacements (dY_1 , dY_2) required to be reproduced by the two control points on the flexible skin are sent to the controller. This controller sends an analogue signal of 0–2 V to the power supply that provides a current to the SMA. The SMA responds accordingly and changes its length according to the temperature of the wire. This will result in a change in

the actuator positions, which are in turn sensed by the LVDT. The signal position received from the LVDT is compared to the desired position and the error obtained is fed back to the controller. If the realized position is greater than the desired position, the controller disconnects the current controller to let the SMA wire to cool down. During the cooling process, the SMA maintains its length due to hysteretic behaviour. This effect is taken into account for the actuators' displacement. The controller uses three

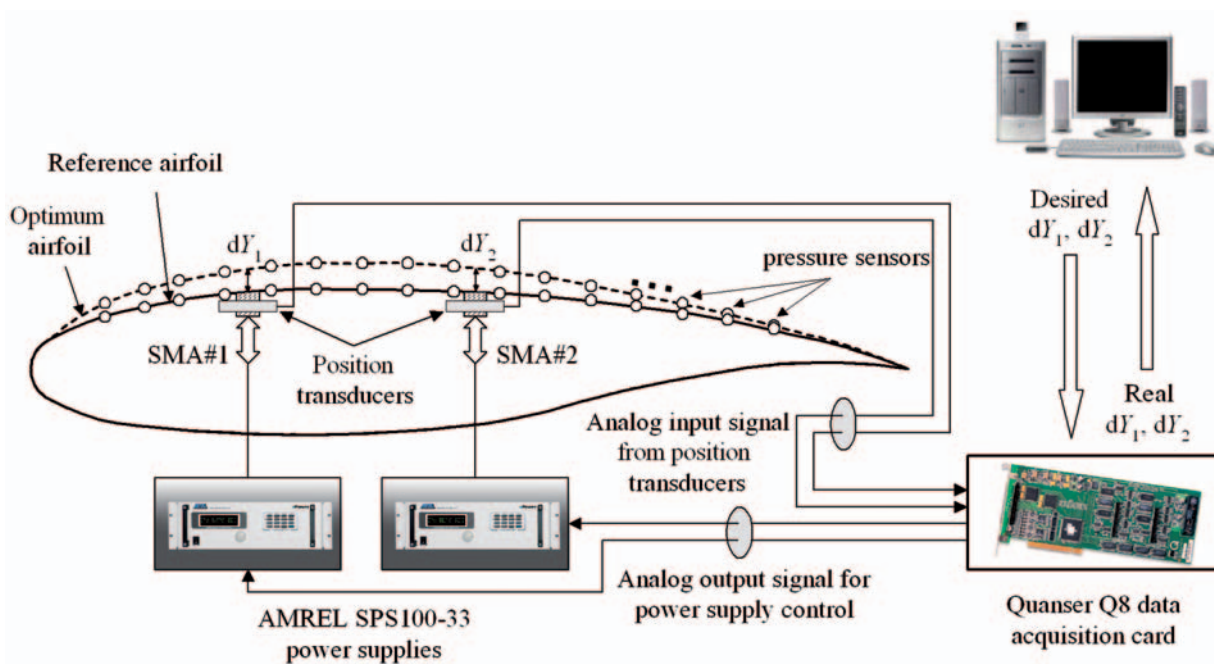


Fig. 10 Bench test physical model operating schema

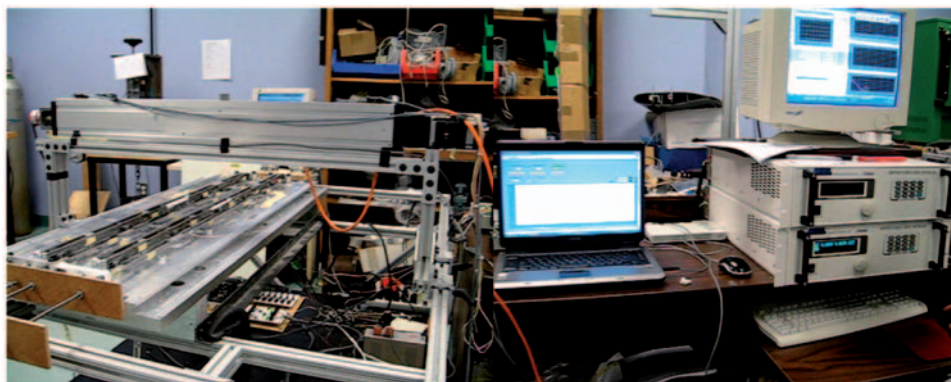


Fig. 11 Morphing wing system in the bench test runs

thermocouple signals from each SMA wire to monitor the temperature and maintain it below 130°C, as an upper limit.

After an initial calibration test, the calibration gains and constants were established for the two LVDT potentiometers and for the six thermocouples (see the values in Fig. 13 for the first SMA actuation line). The calibration test for the LVDT potentiometers consisted of several airfoil scans, using a laser beam. For calibration, the SMA actuators were in the ‘zero setting position’ with no power supplied and the skin coordinates were measured using the laser beam that scanned the centre-line of the wing model. The laser was set to scan the chord of the

model on a 370 mm length with a speed of 5 mm per second.

In a first phase of the bench test, each of the two lines were controlled independently in time to obtain a 7 mm vertical actuated distance ($dY_1 = dY_2 = 7 \text{ mm}$) (Fig. 14). Observation revealed that the controllers, in the two actuation lines, work even at zero values of the desired signal because of the gas spring’s pre-tension load. Also, small oscillations of the obtained deflection are observed around the desired values. The amplitude of the oscillations in this phase is due to the LVDT potentiometers’ mechanical link and to the thermal inertia of the SMA wires; the smallest one is than 0.05 mm. The heating phase is

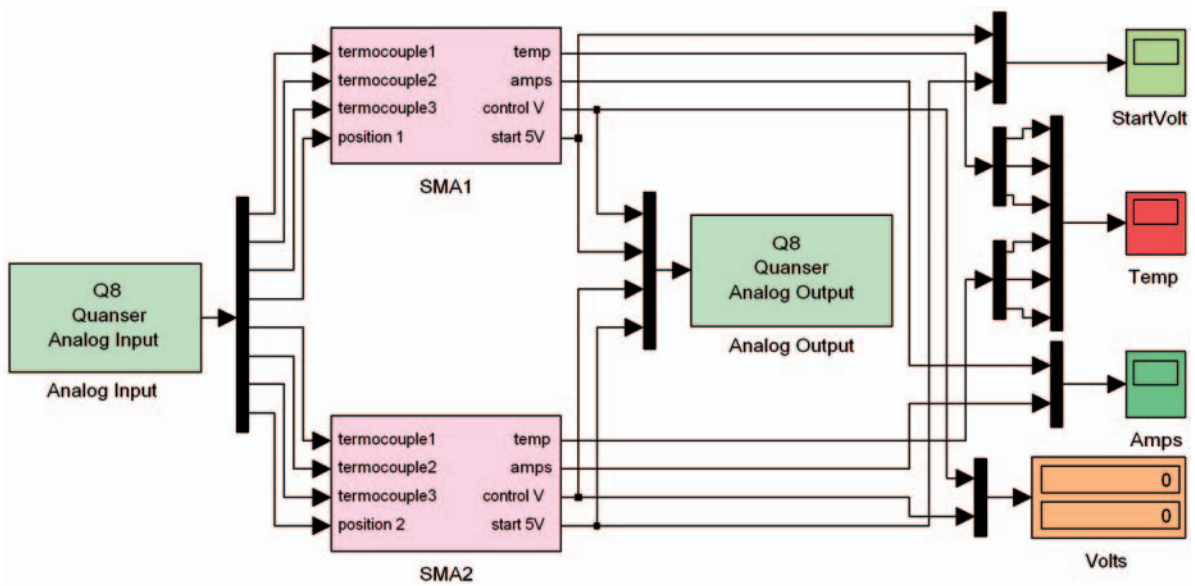


Fig. 12 MATLAB/Simulink actuator control in bench test

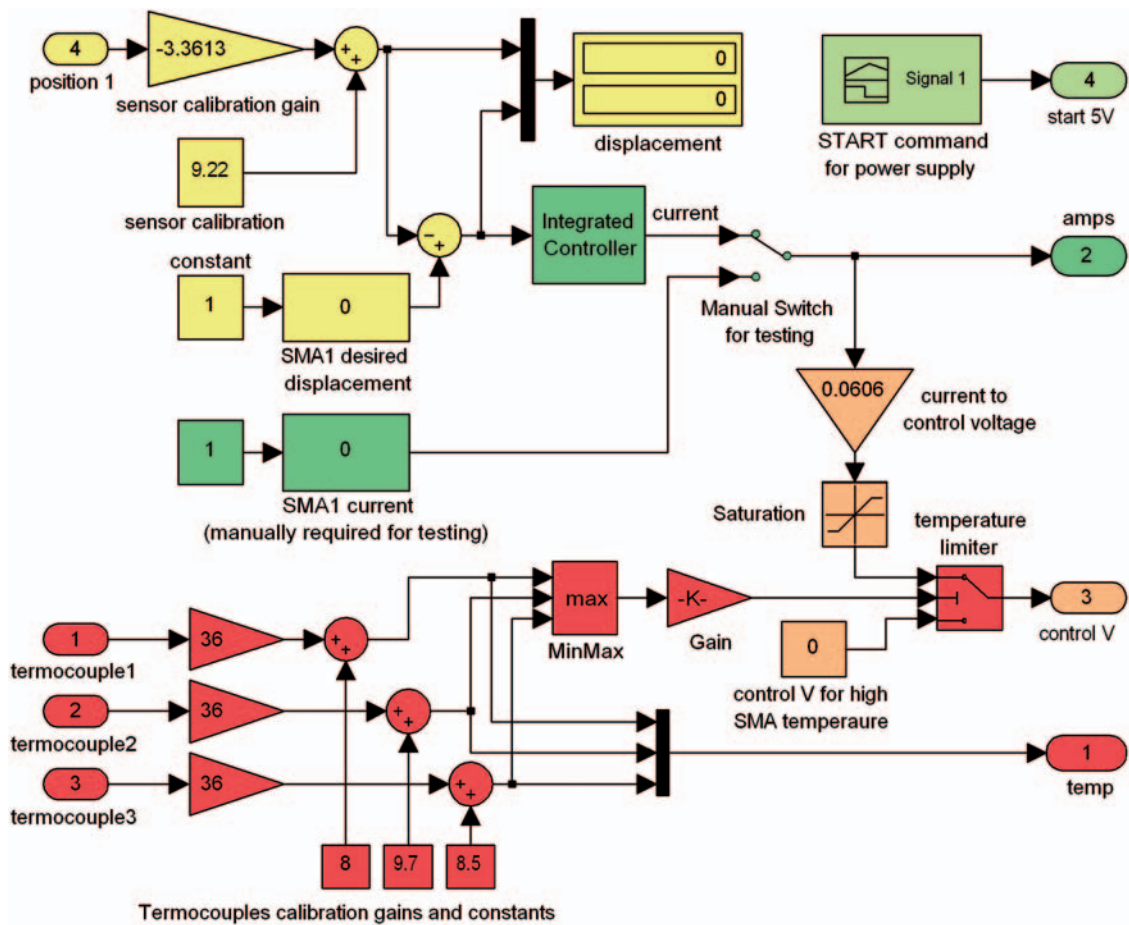


Fig. 13 Schema of the 'SMA1' block

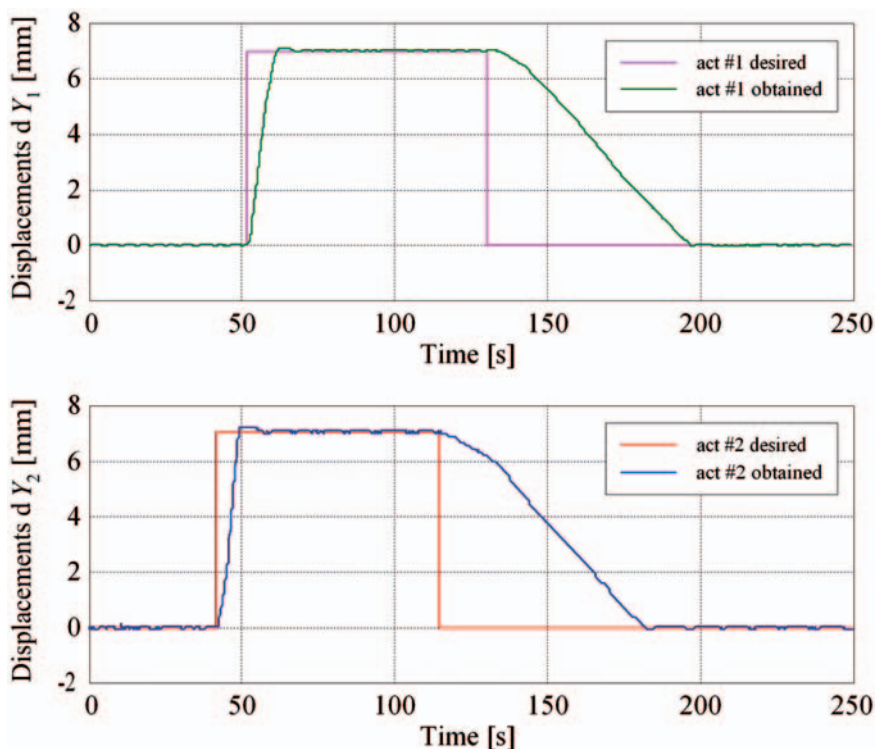


Fig. 14 Bench test for $dY_1 = dY_2 = 7$ mm desired displacements

approximately nine times more rapid than the cooling phase; heating time is 8 s while the cooling time is 70 s. Internal ventilation of the morphing wing model would decrease the SMA cooling time very much. Differences can be observed between the numerical model of the SMA actuators and the physical model.

After that initial test phase, the 35 optimized airfoil cases obtained were converted into vertical displacements for SMA actuators #1 and #2, which were used as input references for the controller. A typical test run history is shown in Fig. 15 for $\alpha = 0^\circ$, Mach = 0.225, $dY_1 = 2.62$ mm and $dY_2 = 4.47$ mm, and in Fig. 16 for $\alpha = 1^\circ$, Mach = 0.3, $dY_1 = 5.22$ mm and $dY_2 = 7.54$ mm. From the numerical values, it is observed that the position control error due to the heating-cooling cycles when the actuator maintains at a desired position is smaller than 0.05 mm.

The bench test results confirmed that the experimental version of the designed integrated controller works well in the laboratory conditions, where no aerodynamic forces are present and the preloaded gas spring's force is 1000 N. Therefore, the observations made in the design phase of the controller, in section 4, including the assumptions related to the optimum value of the SMA load force of around 1000 N, were confirmed. In the next section, a wind tunnel validation test for integrated controller is presented.

4 WIND TUNNEL VALIDATION TEST FOR ACTUATORS' INTEGRATED CONTROLLER

With the confirmed good performance of the designed integrated controller, demonstrated on bench testing, the next step in our morphing wing project was to validate the controller in a wind tunnel test with simultaneous real-time detection of the transition point and visualization for all the 35 optimized airfoils. The model (Fig. 17) was tested for all 35 theoretical flight conditions, with a comparative study realized based on the transition point position for the reference airfoil and for each optimized airfoil. Thus, a validation study for the aerodynamic part of the project was realized at the same time as the controller testing.

The transition location detection was performed using infrared (IR) thermography visualization. The transition detection method using IR is based on the differences in laminar and turbulent convective heat transfer coefficients. In the resulting images, the sharp temperature gradient separating the high temperature (white intensity in image) and the low temperature (dark intensity) regions is an indication of the transition location. The Agema SC3000 camera IR camera, equipped with a 240×320 pixels QWIP detector, was used. It is operating in the IR wavelength region 8–9 μm and cooled to 70°K to reduce

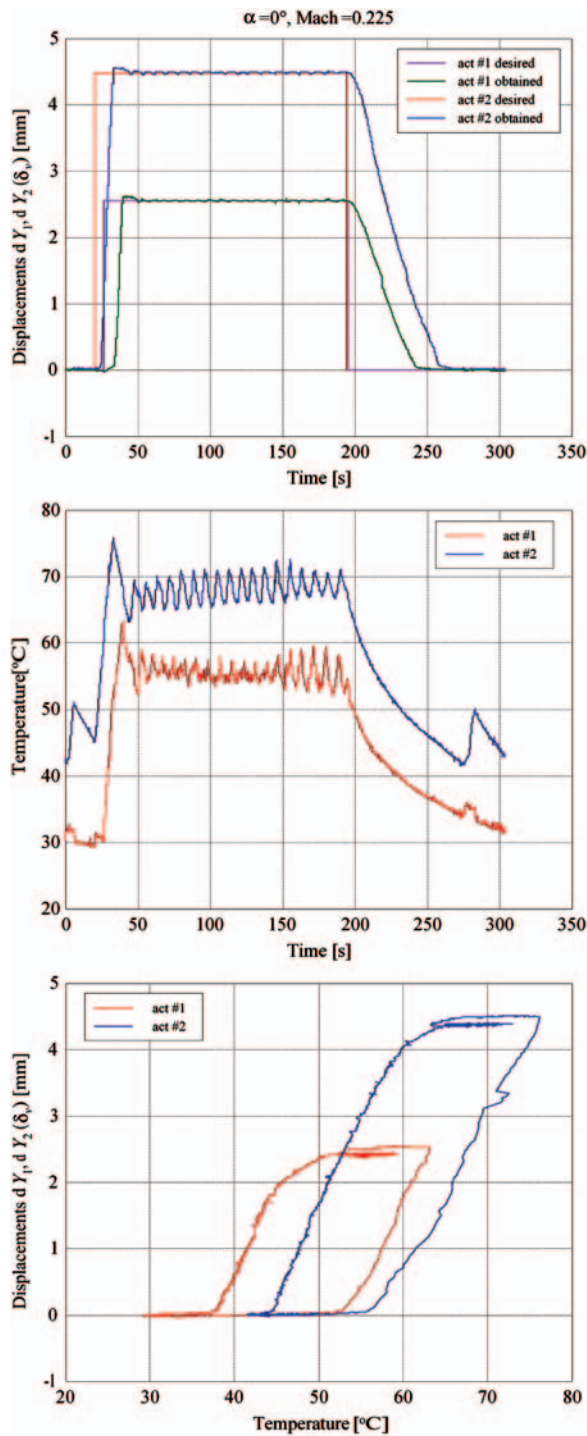


Fig. 15 Bench test for $\alpha = 0^\circ$ and $M = 0.225$

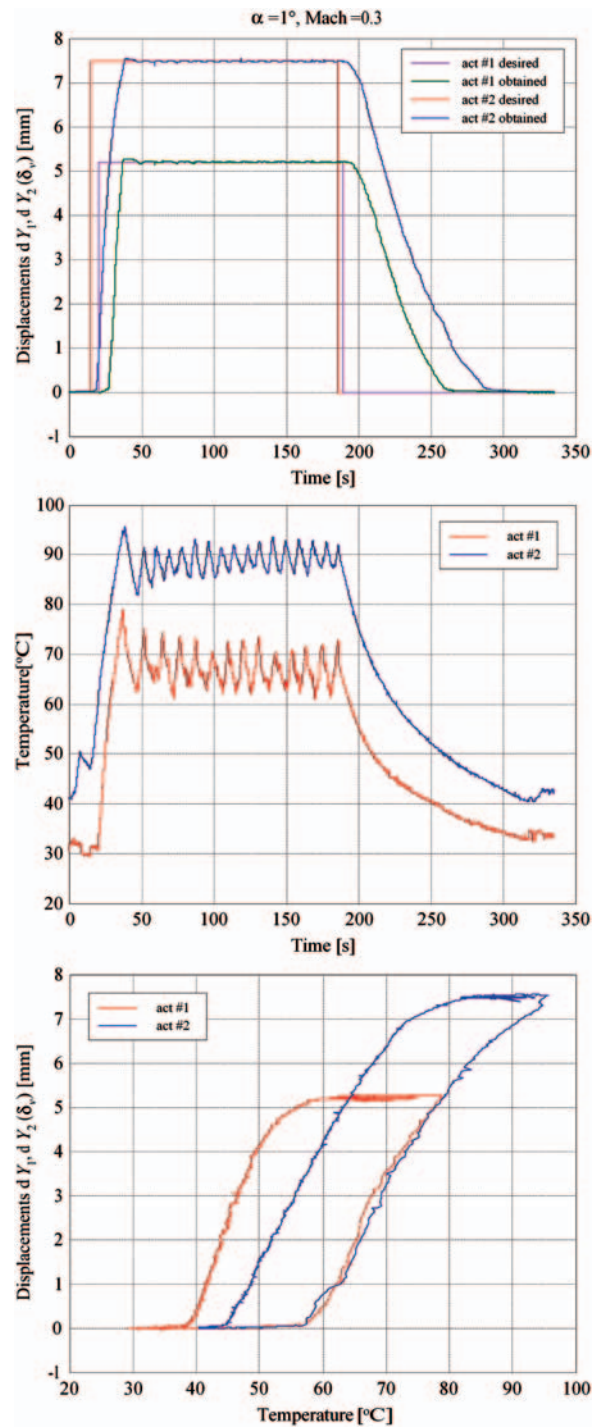


Fig. 16 Bench test for $\alpha = 1^\circ$ and $M = 0.3$

thermal noise. The camera provided a resolution of 0.02°C and a maximum frame rate of 60 samples per second. It was equipped with the default lens ($\text{FOV} = 20^\circ \times 15^\circ$), and was installed 1.5 m away from the model with an optical axis oriented in the horizontal plane at about 30° with respect to the wing surface mid-chord normal. More details about the methodology and processing are available in reference [11].

Figure 18 shows the typical IR results obtained at $M = 0.275$, $\alpha = 0.5^\circ$ for various configurations. Only the composite portion of the wing at $x/c \leq 0.7$ is shown. The white spots on the wing are the electronically heated Kulite pressure transducers. The two lines of SMA actuators, colder than the model surface, are also visible at quarter chord and near mid-chord. The locations of the transition in the images have

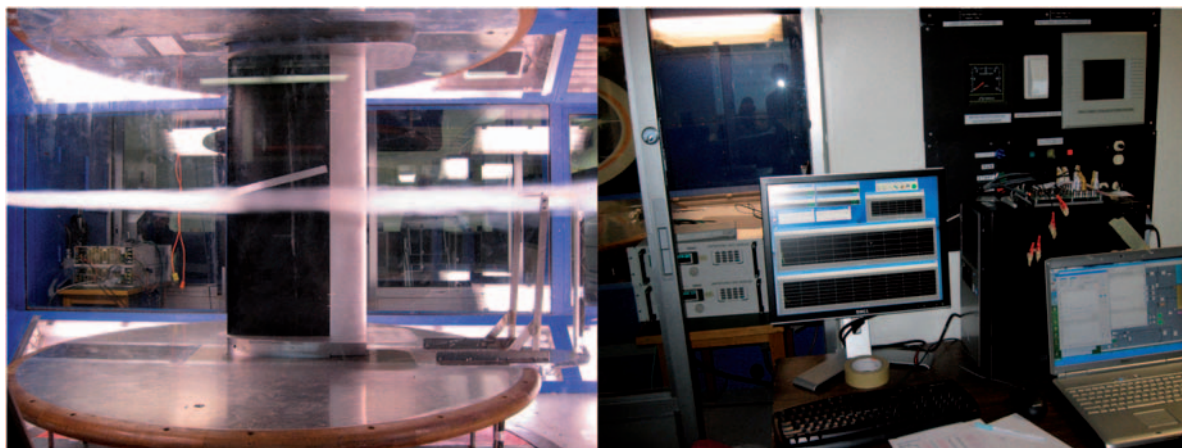


Fig. 17 Wind tunnel morphing wing model

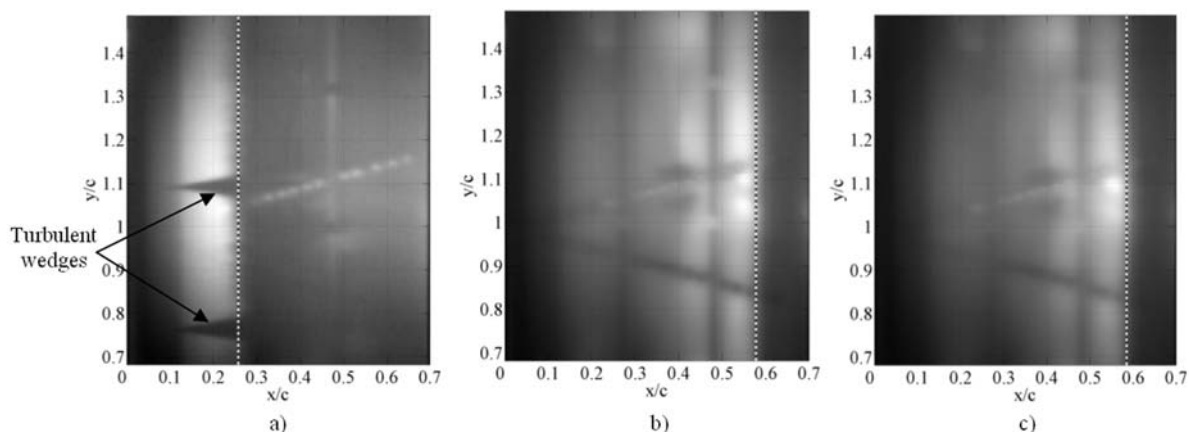


Fig. 18 C225 IR results obtained at $M = 0.275$ and $\alpha = 0.5^\circ$ in: (a) reference, (b) open loop control, and (c) closed loop control

been highlighted using a white dashed line: it corresponds to the location of a large surface temperature gradient, where the laminar region is hotter than the turbulent region by about 2–3 °C. The reference airfoil configuration (Fig. 18(a)) showed a transition location at $x/c = 26$ per cent. The open-loop control (Fig. 18(b)) allowed a laminar boundary layer run to $x/c = 58$ per cent. In the case of the closed-loop control (Fig. 18(c)), the transition location as detected by the IR was also $x/c = 58$ per cent, which represents a significant improvement over the reference case (Fig. 18(a)). Some turbulent wedges are visible owing to surface contamination.

The transition detection was performed in real time using the pressure data signals obtained from the 32 Kulite and optical pressure sensors. The pressure data were acquired using the IAR-NRC analogue data acquisition system, which was connected to the 32 sensors. The sampling rate of each channel was at kept 15 kHz, which allowed a pressure fluctuation

fast Fourier transforms (FFT) spectral decomposition of up to 7.5 kHz for all channels. The signals were processed in real time using Simulink. The pressure signals were analysed using FFT decomposition to detect the magnitude of the noise in the surface air flow. Subsequently, the data were filtered by means of high-pass filters and processed by calculating the root mean square (r.m.s.) of the signal to obtain a plot diagram of the pressure fluctuations in the flow boundary layer. This signal processing is necessary to dispartate the inherent electronically induced noise, by the Tollmien–Schlichting waves that are responsible for triggering the transition from laminar flow to turbulent flow. The measurements showed that in the processed data, the transition appeared at frequencies between 3 and 5 kHz and the magnitudes of the pressure variations in the laminar flow boundary layer are in the order of $5e-4$ Pa. The transition from the laminar flow to turbulent flow was shown by an increase in the pressure fluctuation,

which was indicated by a drastic variation of the pressure signal r.m.s.

For the wind tunnel test, the preloaded forces of the gas springs were reconsidered and increased to 1500 N because of the presence of the aerodynamic forces on the flexible skin of the wing. The control results for two test runs ($\alpha = 1^\circ$ and Mach = 0.2 with $dY_1 = 4.27$ mm and $dY_2 = 7.08$ mm, and $\alpha = 2^\circ$ and Mach = 0.225 with $dY_1 = 5.56$ mm and $dY_2 = 7.91$ mm) are presented in Figs 19 and 20, respectively.

In the wind tunnel closed-loop test, all actuation combinations for dY_1 and dY_2 displacement, between 0 and 8 mm, were considered. The incremental lengths of displacements were set to 2 mm. The system's response for each displacement repeated test is shown in Fig. 21. All the desired displacement values were obtained through actuation which prove that the estimated calculus of the aerodynamic forces in different flight conditions, the chosen pretension gas spring forces, and the elastic coefficient of the flexible skin were very well correlated.

The experimental results show in the work temperatures of SMA wires *vis-à-vis* those observed in the numerically simulated and bench tested cases. This could be explained by the appearance of the aerodynamic forces with different values for each flight condition. The decrease of the temperatures is beneficial while considering the negative impact of high operating thermal on the system components and instrumentations (the flexible skin and the pressure sensors).

Also, from the experimental results, a high-frequency noise influencing the LVDT sensors and the thermocouple's instrumentation amplifiers is observed. The noise sources are the wind tunnel vibrations and the instrumentation electrical fields. Even with this noise, the amplitude of the actuation error is less 0.07 mm, and this does not affect the transition location, which remains stable as detected by the sensor having a high r.m.s. spike.

Figure 22 presents the results obtained by the transition monitoring for the run test in Fig. 20. The actuation line control precision can have some influence on the transition location detection only if the density of the chord-disposed pressure sensors becomes greater. From the processed experimental data, it is concluded that, even if the value of the error is 1 mm around the optimized values, the transition location on the flexible skin is not significantly changed. The real-time Kulite pressure signals and their r.m.s. are presented in Fig. 22. The left-hand column shows the results for the reference airfoil, and the right-hand side column the results for the optimized airfoil. The spike of the r.m.s. suggests that the flow has

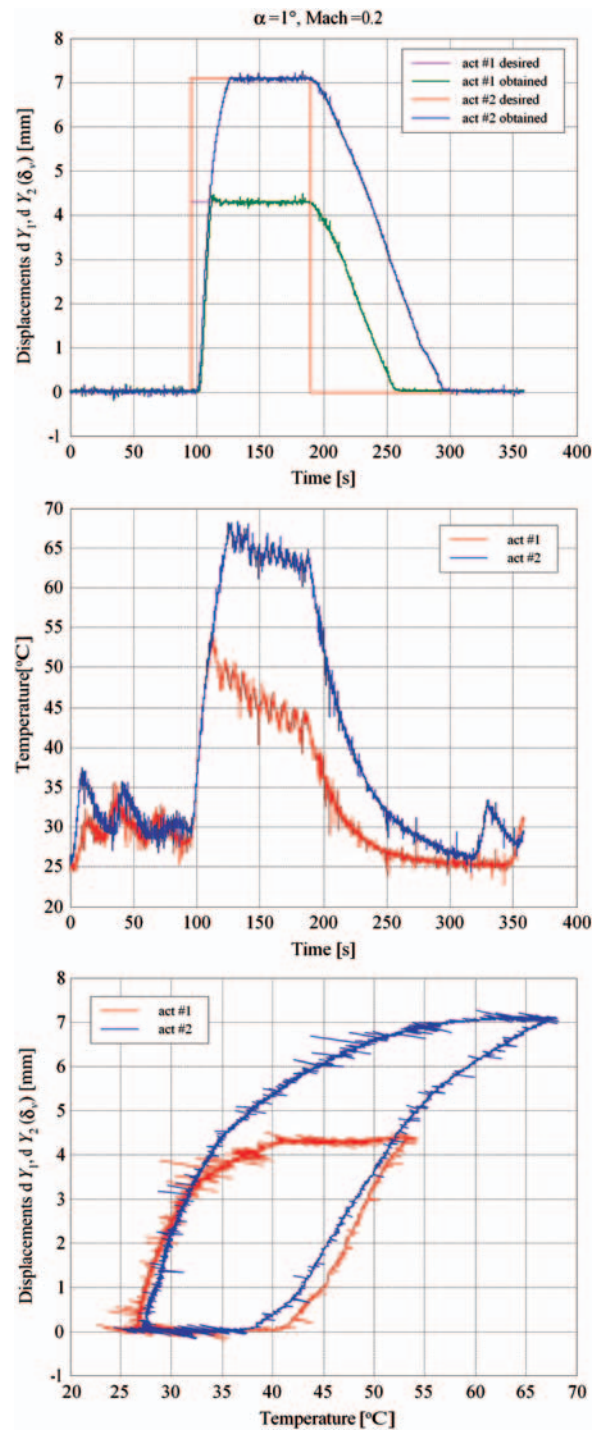


Fig. 19 Wind tunnel test for $\alpha = 1^\circ$ and $M = 0.2$

already turned turbulent on sensor no. 12, near the trailing edge.

The results obtained from the wind tunnel tests show that the actuator control – and the controller performed very well in enhancing the wind aerodynamic performance and fully satisfy the project requirements.

Future work on this project will focus on developing the closed-loop control, based on the pressure

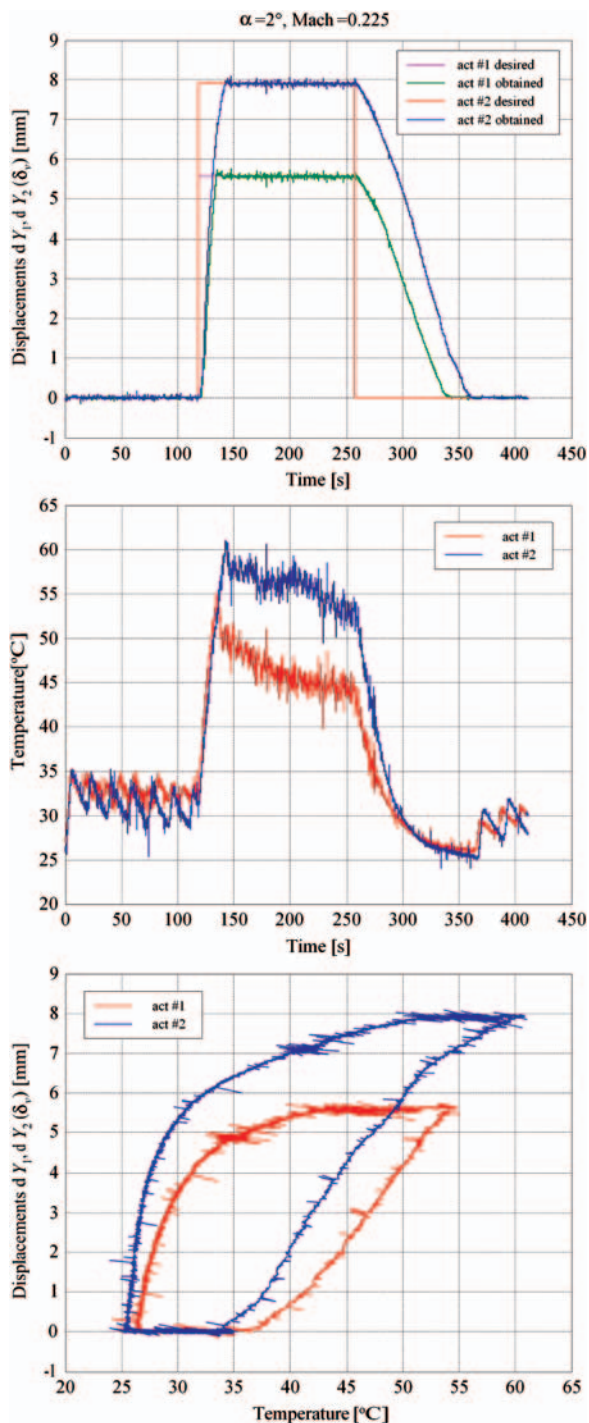


Fig. 20 Wind tunnel test for $\alpha = 2^\circ$ and $M = 0.225$

information recorded by sensors and on the transition location estimation. The closed-loop control will certainly include, as an internal loop, the actuation lines controller presented in this study.

5 CONCLUSIONS

This article represents the second part of a study related to the development of an actuator control

system for a morphing wing application, and describes the numerical and experimental validation of the control designed in the first part. The control experimental validation was made in two ways: bench test and wind tunnel test.

In the numerical simulation section, the integrated controller was validated with the MATLAB/Simulink program package. The transition to the desired steady state is significantly improved through the integration of the two control laws in equation (1): (1) the amplitudes of oscillations were reduced and the observed oscillations in the SMA temperatures around the steady state are due only to the thermal inertia of the smart material and (2) the values of the transition time from 0 mm to the steady state values decrease from 20 to 25 s (values obtained in the first part of the study – pre-design phase) to approximate 5 s. Another positive consequence attributable to a F_{aero} increase is the decrease in the work temperature of the SMA actuators. The advantage of lower temperature is twofold: (1) a lower temperature allows rapid cooling and (2) the interaction between the actuators and the other parts of the physical model will be within normal limits. From another point of view, the F_{aero} increase produces an increase in the initialization phase. From simulations, it is observed that a high F_{aero} value produces a low load force F_{SMA} and the actuators do not work properly. Therefore, by estimating the aerodynamic forces for all 35 studied flight conditions and 35 optimized airfoils, a compromise must be made to balance with the preloaded forces of the gas spring. The preloaded forces on the gas springs in the two actuation lines must be generally valid for all the cases studied. Hence, the actuators must be seriously loaded to work well ($F_{pretension}$ higher so that F_{SMA} is higher), but the load must not be too high because it becomes non-deformable if the aerodynamic forces are not so stronger and able to counterbalance it.

In a first phase of the bench test, each of the two lines was controlled independently in time. The bench test results confirmed also that the experimental version of the designed integrated controller works well even in laboratory conditions, where no aerodynamic forces are loaded.

The final validation test (wind tunnel test), with a real aerodynamic force load, shows a decrease of the SMA wires' work temperatures *vis-à-vis* those for the numerically simulated and bench tested cases. The decrease of these temperatures is beneficial when accounting for the negative impact of a strong thermal field on the other system components, especially on the flexible skin and on the pressure sensors. Also, a high-frequency noise influencing the LVDT sensors and the thermocouples' instrumentation amplifiers

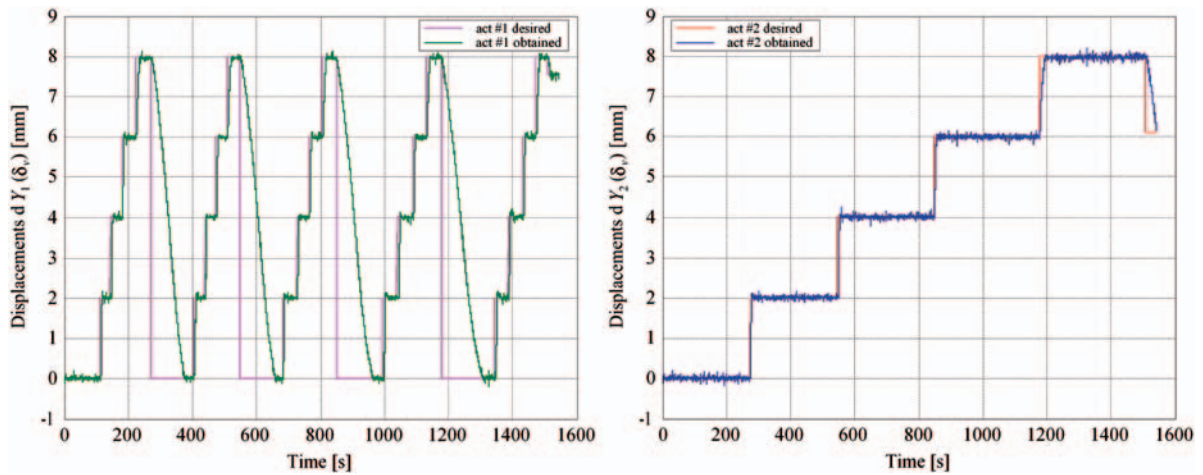


Fig. 21 Actuation results for repeated steps, simultaneously applied on the two actuation lines

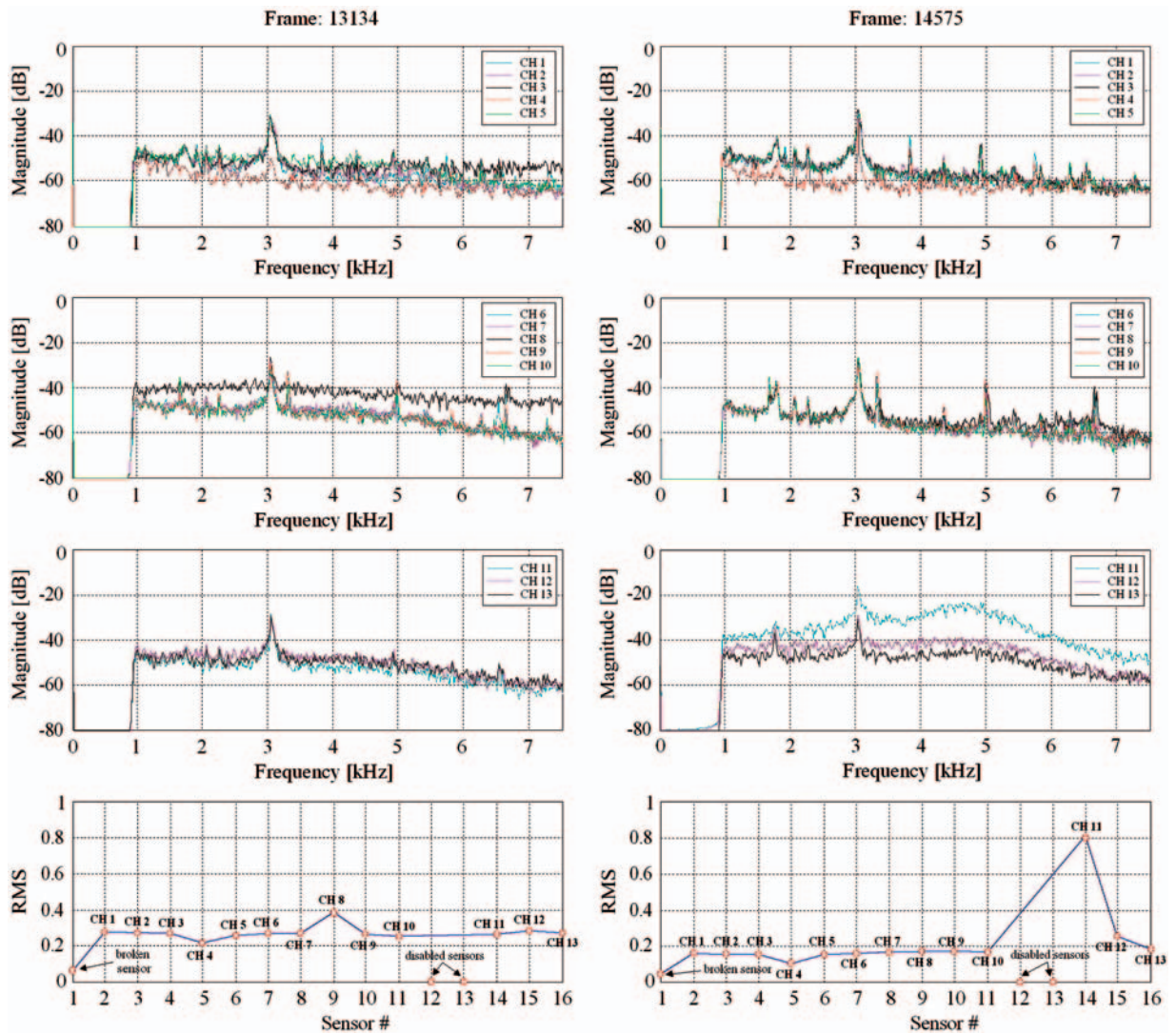


Fig. 22 Results obtained on the transition monitoring for the run test in Fig. 20

can be observed. The noise sources are the wind tunnel vibrations and the instrumentation's electrical fields. The wind tunnel test proves that *the estimative calculus of the aerodynamic forces* appearing on the airfoil in different flight conditions, *the chosen pretension gas spring's forces* and *the elastic coefficient of the flexible skin* were very well correlated.

Overall, the results obtained for the actuators' control are very good, the controller fully satisfying the requirements imposed for the project's purpose.

The designed controller is used for the open-loop development stage of a morphing wing project, but the closed loop of the morphing wing system, based on the pressure information received from the sensors and on the transition point position estimation, will include, as an internal loop, the actuation lines controller presented here.

ACKNOWLEDGEMENTS

The authors thank the Consortium for Research and Innovation in Aerospace in Quebec (CRIAQ), Thales Avionics Inc., Bombardier Aerospace, and the National Sciences and Engineering Research Council (NSERC) for their financial support. We also thank Dr George Henri Simon for initiating the CRIAQ 7.1 project and Dr Philippe Molaret from Thales Avionics and Dr Eric Laurendeau from Bombardier Aerospace for providing help and facilitating fruitful discussions.

© Authors 2011

REFERENCES

- 1 **Smith, K., Butt, J., Spakovsky, M. R., and Moorhouse, D. A.** Study of the benefits of using morphing wing technology in fighter aircraft systems. In Proceedings of the 39th AIAA Thermophysics Conference, Miami, Florida, USA, 25–28 June 2007.
- 2 **Hinshaw, T. L.** *Analysis and design of a morphing wing tip using multicellular flexible matrix composite adaptive skins*. MSc Thesis in Aerospace Engineering, Virginia Polytechnic Institute and State University, 1 July 2009, Blacksburg, Virginia, USA.
- 3 **Chang, P., Shah, A., and Singhee, M.** Parameterization of the geometry of a blended-wing-body morphing wing, The Systems Realization Laboratory, Georgia Institute of Technology, April 2009, Atlanta, Georgia, USA.
- 4 **Gonzalez, L.** Morphing wing using shape memory alloy: a concept proposal, Final research paper in 2005 Summer Research Experience for Undergraduates (REU) on Nanotechnology and Materials Systems, Texas Institute of Intelligent Bio-Nano Materials and Structures for Aerospace Vehicles (TiiMS) - NASA Research University, Texas A&M University, July 2005, College Station, Texas, USA.
- 5 **Namgoong, H., Crossley, W. A., and Lyrintzis, A. S.** Aerodynamic optimization of a morphing airfoil using energy as an objective. In Proceedings of the 44th AIAA Aerospace Sciences Meeting and Exhibit, Reno, Nevada, USA, 9–12 January 2006.
- 6 **Majji, M., Rediniotis, O. K., and Junkins, J. L.** Design of a morphing wing: modeling and experiments. In Proceedings of the AIAA Atmospheric Flight Mechanics Conference and Exhibit, Hilton Head, South Carolina, USA, 20–23 August 2007.
- 7 **Ruotsalainen, P., Kroneld, P., Nevala, K., Brander, T., Lindroos, T., and Sippola, M.** Shape control of a FRP airfoil structure using SMA-actuators and optical fiber sensors. *J Solid State Phenom*, 2009, **144**-Mechatronic Systems and Materials II, 196–201.
- 8 **Kirianaki, N. V., Yurish, S. Y., Shpak, N. O., and Deynega, V. P.** *Data acquisition and signal processing for smart sensors*, 2002 (John Wiley & Sons, Chichester).
- 9 **Park, J. and Mackay, S.** *Practical data acquisition for instrumentation and control systems*, 2003 (Elsevier, Oxford).
- 10 **Austerlitz, H.** *Data acquisition techniques using PCs*, 2003 (Elsevier, USA).
- 11 **Mébarki, Y., Mamou, M., and Genest, M.** Infrared measurements of transition location on the CRIAQ project morphing wing model, NRC LTR- AL-2009-0075, National Research Council, Ottawa, Ontario, Canada, 2009.

APPENDIX

Notation

c	chord
c_f	cam factor
dY_{1opt}	optimal vertical displacement of actuator 1
dY_{2opt}	optimal vertical displacement of actuator 2
dY_{1real}	real vertical displacement of actuator 1
dY_{2real}	real vertical displacement of actuator 2
e	actuation loop error
F_{aero}	aerodynamic force
$F_{pretension}$	pretension spring force
F_{SMA}	resultant force that acts on the SMA
$i(t)$	command variable (electrical current)
M	Mach number
PI	proportional–integral
Re	Reynolds number
t	time
x	horizontal stroke
z	vertical stroke
α	angle of attack
δ_h, δ_v	horizontal and vertical actuated displacements